

TRAJECTORY DENSIFICATION AND DEPTH FROM PERSPECTIVE-BASED BLUR

Tianchen Qiu, Qirun Zhang, Jiajian He, Zhengyue Zhuge, Jiahui Xu, Yueling Chen*

College of Optical Science and Engineering
Zhejiang University
Hangzhou, China

{12530010, zhangqirun, hejiajian2, zgzy, xu_jiahui, chenyt}@zju.edu.cn

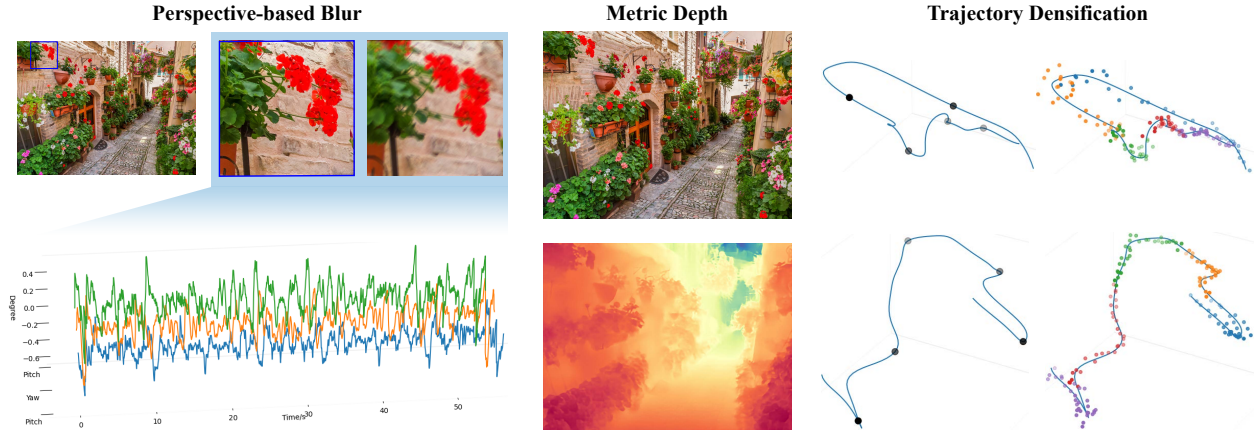


Figure 1: Our method predicts metric depth map and dense trajectory within frames from perspective-based blur, which is caused by camera motion located on the curve of left above. In the trajectory densification part, the left column depicts the computed sparse trajectory, whereas the right column shows the predicted dense one; the blue solid line denotes the ground truth(GT).

ABSTRACT

In the absence of a mechanical stabilizer, the camera undergoes inevitable rotational dynamics during capturing, which induces perspective-based blur especially under long-exposure scenarios. From an optical standpoint, perspective-based blur is depth-position-dependent: objects residing at distinct spatial locations incur different blur levels even under the same imaging settings. Inspired by this, we propose a novel method that estimate metric depth by examining the blur pattern of a video stream and dense trajectory via joint optical design algorithm. Specifically, we employ off-the-shelf vision encoder and point tracker to extract video information. Then, we estimate depth map via windowed embedding and multi-window aggregation, and densify the sparse trajectory from the optical algorithm using a vision-language model. Evaluations on multiple depth datasets demonstrate that our method attains strong performance over large depth range, while maintaining favorable generalization. Relative to the real trajectory in handheld shooting settings, our optical algorithm achieves superior precision and the dense reconstruction maintains strong accuracy.

1 Introduction

Inferring camera motion from multiple images has been an essential task in computer vision community, for which structure-from-motion (SfM) methods have achieved substantial progress[1, 2, 3, 4]. That said, most existing approaches emphasize camera position estimation on a per-image basis, while the accompanying view-angle differences are generally considerable. With the growing adoption of telephoto optical lenses on mobile platforms, imaging without

an external stabilizer becomes susceptible to pronounced blur, primarily driven by camera shake. Furthermore, the in-module optical stabilization system is subject to inherent limitations, such as temporal response lag and residual imaging shift, that introduce perspective-based blur[5, 6]. In this regime, pipelines from the SfM literature fall short in producing dense motion trajectory and fail to converge reliably for small-magnitude motions.

From optical standpoints to obtain high-precision sparse trajectory, access to the scene depth map is indispensable. Depth estimation is a mature line of work that includes metric and relative depth, single image and video streams[7, 8, 9, 10]. Notably, most motion-based approaches target the recovery of relative depth[11]; however, for an accurate camera optics model, metric depth is required. Accordingly, to reconstruct metric depth, they are often integrated with monocular depth prediction methods, producing a dense metric depth map.

Our work propose a novel jointly optical pipeline based on local blur features from monocular video streams, aggregating relative depth information within single temporal window across multiple windows to obtain metric depth map, and condensing trajectory, which is resulted from optics-based algorithm, via vision-language model. The video stream is encoded with a shared vision Transformer[12], upon which we attach heterogeneous decoders to derive task-dependent results. Specifically, considering the vision input of trajectory densification, we route the encoded features through the depth stage’s self-attention layers on a per-frame basis, concatenate them with the terminal depth-decoder predictions. For training process, we first focus on parameters of depth stage, then train the trajectory stage while freezing the former, only for inference. Ground-truth depth is sourced from the depth datasets, while the trajectory one corresponds to the input curves used during video simulation[13, 14].

We extensively evaluate our method on diverse datasets, including indoor, outdoor, distant, realistic, and synthetic scenarios. Both quantitative results of depth estimation and trajectory densification demonstrate that our pipeline achieves state-of-art performance compared with other video depth estimators, outperforming existing SfM methods in terms of the temporal density and accuracy of camera motion. This main contributions of this work are summarized below:

- We innovate a novel method to reconstruct metric depth map from streaming video sequences, by analyzing the evolution of perspective-based blur across temporal frames, outperforming video depth estimators.
- We propose an optics-based camera trajectory algorithm that leverages a point tracker to obtain delta of predefined points, yielding a frame-by-frame camera trajectory. It exhibits improved accuracy over other methods when evaluated in the small-angle regime.
- We present a two-stage strategy to enable generating dense trajectory, fusing sparsely sampled sequence from first stage and video vision information, in the second stage. It attains strong accuracy when compared against ground truth.

2 Related Work

Structure from motion. SfM aims to jointly recover camera poses and sparse 3D structure from unordered 2D images. Early theoretical development established the fundamentals of multi-view geometry[15, 16, 1] and bundle adjustment(BA)[17]. Classical incremental pipelines, such as Photo Tourism[18], demonstrated Internet-scale 3D reconstruction by sequentially registering views and triangulating 3D points. Practical SfM systems like VisualSf[19] and COLMAP[2] combined robust two-view estimation[20, 21] with Levenberg–Marquardt(LM) BA[22] to deliver highly accurate sparse reconstructions. Despite their reliability, incremental methods suffer from drift accumulation and are computationally expensive for large-scale datasets. To address this, global SfM methods estimate all camera orientations and positions in a unified optimization framework. Representative approaches include 1DSfM[23], which performs robust rotation averaging via pairwise 1D projections, and TheiaSfM[24], which jointly refines camera positions using robust cost aggregation. Hybrid pipelines such as OpenMVG[25] combine global initialization and incremental refinement to ensure global consistency with local precision.

Learning-based SfM has recently emerged to integrate geometric reasoning with deep supervision for better scalability and generalization. DeepSfM[26] and BA-Net[27] embed deep networks into classical BA pipeline. DUS3R[3] directly predicts 3D pointmaps from pairs of input images, demonstrating strong generalization across diverse scenarios. Extending this framework, MAS3R[28] incorporates an additional feature extraction head that enables dense pixel-level correspondence estimation. With more neural representations[29, 30], geometry-based SfM is increasingly integrated with neural implicit modeling, improving both accuracy and convergence robustness.

Feature point tracking. Feature tracking is critical for accurate pose estimation and matching in classical SfM pipelines[31, 32, 33]. Traditional methods relied on optical flow[34] and KLT trackers[35], while modern dense and sparse descriptors[36, 37, 38] enhanced detection robustness. Modern works go beyond hand-crafted descriptors, introducing learning-based point-tracking frameworks that explicitly model temporal or spatial coherence.

The Track Any Point (TAP) family of methods[39, 40, 41, 42, 43, 44] improved general-purpose point tracking by constructing dense spatio-temporal correlation volumes. TAP-Net[40] computed a global cost volume and applied convolutions followed by a soft-argmax for trajectory estimation, while PIPs[41] iteratively refined track trajectories

through MLP-Mixer[45] modules. TAPIR[42] integrated TAP-Net with PIPs for better long-term consistency, and CoTracker[43] exploited self-attention in Transformers[46] to jointly track multiple interacting points in a unified sequence transformer. More recent variants such as TAPTR[44] and LocoTrack[39] enhance correlation computation through local context aggregation, improving multi-object and non-rigid motion robustness.

Monocular depth estimation. Monocular depth estimation (MDE) addresses depth prediction from a single RGB camera. Classical learning-based MDE approaches, such as MegaDepth[47] and MiDaS[48], demonstrated that large and diverse training datasets significantly improve generalization across domains. Recent models employ self-training on unlabeled datasets[49] or use vision foundation backbones such as Stable Diffusion[50] and DINOv2[12] to achieve scale-consistent depth predictions. More recent works, such as DepthAnything[8], leverage large-scale pretraining and temporal feature aggregation to improve continuity and accuracy across dynamic scenes.

3 method

3.1 Theoretical Analysis

In static environments, when the camera undergoes motion, the resulting temporal frames manifest image displacement and exposure-induced blur. For scene content residing on a common depth plane, the variations across different FOVs in the image adhere to a deterministic rule induced by the optical geometry. Natural environments exhibit dense depth variation, wherein the dynamics of temporal frames are systematically linked to the depth of the respective FOV. Under short exposure, inter-frame comparisons in the video suffice to reveal image changes, whereas for long exposures, the magnitude of change manifests as various forms of image blur. Consequently, valuable depth information about the scene and motion parameters of the camera can be inferred from continuous video.

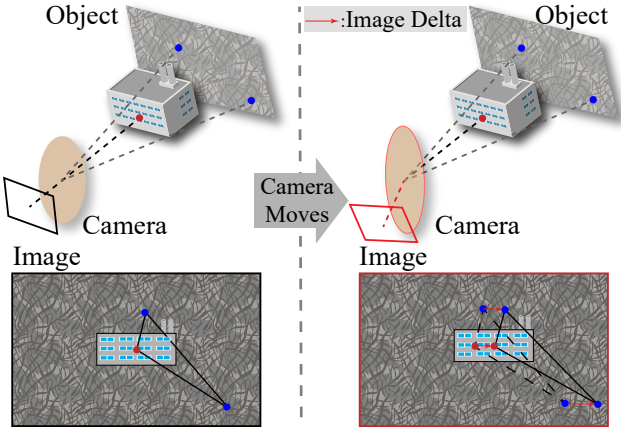


Figure 2: An ideal optical system. Red point is on-axis point and blue points denote off-axis point. Under an identical camera state, scene points at different spatial locations exhibit different image deltas.

Formally, given a RGB video with T frames, we primarily focus on the temporal evolution of selected N query points; specifically, these points are fields-of-view sampled uniformly over the first frame of the video. As the camera shakes over time, query points shift, and their local neighborhoods exhibit particular blur patterns. The spatio-temporal delta of query points, their corresponding object distances and camera motion trajectory are parameterized as:

- **Delta:** $\Delta = \{\delta_i\}_{i=1}^N$, where each $\delta_i = \{(p_x, p_y)_{i,t}\}_{t=1}^T$ consists of the 2D positional coordinate displacement of query point i across T frames.
- **Depth:** $L = \{l_i\}_{i=1}^N$, where l_i indicates the metric depth of query point i at the first frame.
- **Trajectory:** $\Theta = \{\theta_t\}_{t=1}^T$, where $\theta_t = \{(\alpha, \beta, \gamma)_t\}$ encapsulates three parameters of the camera rotation at the t frame.

Within an ideal optical imaging system, we consider a query point Q_{on} at central FOV and another query point Q_{off} at an off-axis FOV, with the sensor located at the conjugate plane of the on-axis point. Each point is further expanded into a small neighborhood region with patch P_{on} and P_{off} , at depth $l_{Q_{on}}$ and $l_{Q_{off}}$. At time t , the camera's rotational state is three-dimensional and we construct the plane defined by the rotation vector and the optical axis. In this plane, the rotation angle is θ_t and the dihedral angles of this plane with respect to the image-plane x- and y-axes are ϕ_x and ϕ_y , respectively. The resulting delta onto the image plane of Q_{on} is given by:

$$\delta_{Q_{on}} = -l_{Q_{on}} \tan\theta_t \frac{f'}{l_{Q_{on}} + f'}, \quad (1)$$

where f' is the focal length of the optical system. Meanwhile, the delta associated with Q_{off} is:

$$\delta_{Q_{off}} = -\frac{l_{Q_{on}} \tan \theta_t}{l_{Q_{off}}} \frac{f'}{l_{Q_{on}} + f'} \frac{l_{Q_{off}} - y^2}{l_{Q_{off}} - y \tan \theta_t}, \quad (2)$$

where y denotes the object height corresponding to Q_{off} . Assuming small path P_{on} and P_{off} have locally uniform displacements $\delta_{Q_{on}}$ and $\delta_{Q_{off}}$ the imaging result of this region in t frame is:

$$G(P) = \frac{1}{t_E} \int_0^{t_E} \iint_{p,q \in P} I(p + (p_x)_t, q + (p_y)_t) dt, \quad (3)$$

where $p_x = \delta_i \cos \phi_x$, $p_y = \delta_i \cos \phi_y$, t_E is the exposure time for each frame and I denotes the image under stationary condition. It follows that the blur ρ of the patches is determined by Δ and a contiguous trajectory denser than Θ . Given identical exposure settings and camera motion for both Q_{on} and Q_{off} , the ratio of ρ between them follows:

$$\frac{\rho_{off}}{\rho_{on}} \propto \frac{\delta_{Q_{off}}}{\delta_{Q_{on}}} = -\frac{1}{l_{Q_{off}}} \frac{l_{Q_{off}} - y^2}{l_{Q_{off}} - y \tan \theta_t}. \quad (4)$$

From Eq. 1 and Eq. 4, ρ_{off} is associated with ρ_{on} , the object's spatial position and the motion trajectory, whereas ρ_{on} depends only on depth and the trajectory. Eq. 3 indicates that the blur magnitude ρ depends solely on the image delta Δ under the same exposure state.

It should be emphasized that the theoretical derivation above assumes near-constant image shift over a local patch and a solid sensor pose during the exposure interval. During depth estimation, the continuous trajectory is impractical to confirm, yet ρ_{on} depends on it linearly. In solving for dense trajectories, as temporal information is hidden during integration, blind restoration exhibits a multi-solution ambiguity.

To address these constraints, we employ a Transformer-based framework, as shown in Figure 3, to extract and compare the complexities across multiple FOV regions and temporally ordered frames through learned representations. Rather than depending exclusively on explicit equation-based computations, the approach infers metric depth of object and dense camera trajectory, thereby improving robustness to variations in motion dynamics.

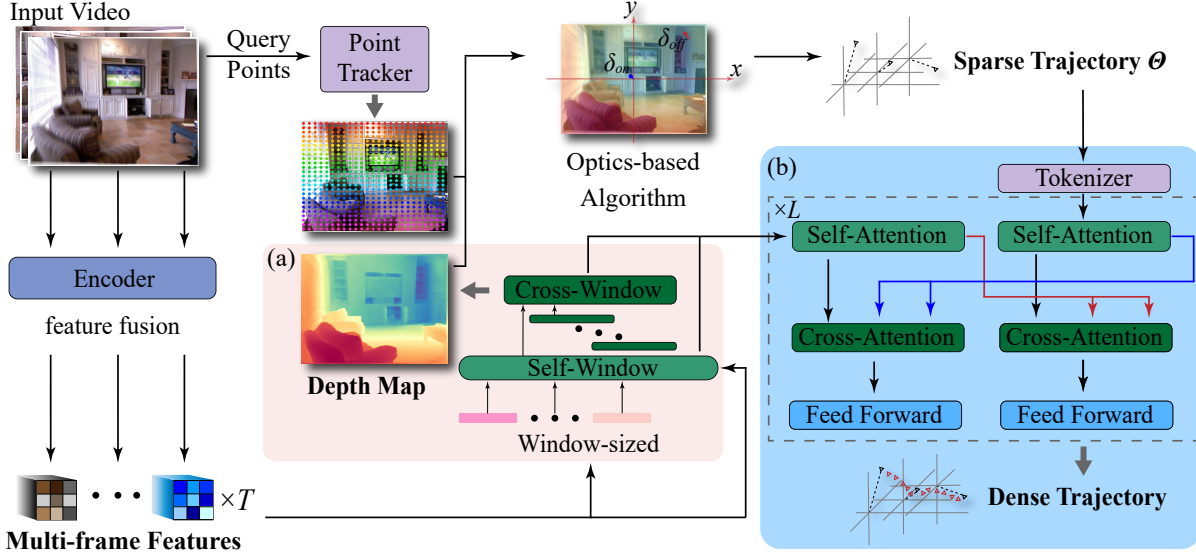


Figure 3: **Overview of our pipeline.** We begin by extracting multi-frame features with DINO[12] model, while employing off-the-shelf point tracker[43] to derive Δ of N query points, from which we compute sparse trajectory Θ via optics-based algorithm. **(a) Depth estimation.** We segment the T -length features into window-size and further encode them with self-attention, followed by aggregation into the first window via cross-attention. **(b) Dense trajectory decoder.** Multi-frame features fused with the depth map L are injected into tokenized[51] Θ , resulting in the dense camera trajectory.

3.2 Video Information Extraction

For effective depth estimation and dense trajectory computation, as discussed in Sec. 3.1, it's crucial that the model firstly captures the per-frame local blur ρ and inter-frame motion trajectory Θ . To address these requires, we employ

DINOv2[12] model to obtain high-dimensional image features and off-the-shelf tracker[43] to estimate the temporal motion of query points.

Multi-frame features. To balance accuracy and computational complexity, we adopt DINOv2(ViT-B) as video encoder. Larger backbones incur higher memory footprints, whereas ViT-S model with fewer attention heads diminish cross-region dependency capture, which is important for our ratio blur pattern computation. For enhancing scale robustness, we gather feature parameters from K different layers of the encoder. Considering a input video $V = \{I_t\}_{t=1}^T$, where $I_t \in \mathbb{R}^{h \times w \times 3}$, the features extracted are $\phi_t = \{\phi_{t,k}\}_{k=1}^K$, where $\phi_{t,k} \in \mathbb{R}^{h_k \times w_k \times d_k}$. As features from different layers differ in spatial resolution and channels, low-resolution features are upsampled and multi-scale features are fused into a unified representation $\phi_t \in \mathbb{R}^{h_1 \times w_1 \times d}$ via linear layers. The final output multi-frame features, denoted as $\Phi = \{\phi_t\}_{t=1}^T$, aggregates per-frame features across time and scales, serving as a rich representation of our required blur pattern.

Query points tracking. In the tracking module, the pretrained point tracking model Cotracker[43] suffices for our single-point tracking requirement. For query points setting, we control its density by count of half-width, while ensuring that the on-axis point is always included. Assuming a half-width count of i , the number of query points $N = (2i + 1)^2$, comprising the on-axis point and other points uniformly sampled in each of the height and width directions. The tracker model yields temporal coordinates for the query points, which we convert into delta Δ relative to the first frame. Since the captured scene remains static and limited camera motion, the visibility term contained in the tracking model output is therefore omitted. Subsequently, an estimation of the sparse camera trajectory Θ can be performed based on the delta Δ and the depth map L .

3.3 Depth Map Estimation

In the depth estimation module, we apply attention over the extracted features and project them through the output layer to a single-channel depth map. The module is simplified in Figure 3, while the layer-wise operations are detailed in Figure 4.

For the input temporal features $\Phi = \{\phi_t\}_{t=1}^T$, we first apply window-embedding to further aggregate ambiguous information. With short exposure time recording, omitting window-embedding leads to performance degradation in the downstream attention computation. Specifically, let S denotes the window length, $\{\phi_t\}_{t=(n-1)S}^{nS}$ are concatenated along the channel dimension, and then use convolutional layers to reduce the channels back to the original size $\phi_t \in \mathbb{R}^{h_1 \times w_1 \times d}$.

Following window-embedding, the features are processed by the *Self – Window* module, which is invoked again during trajectory densification, and the parameters are shared across both uses. This module primarily compares different local regions within the same frame to extract relative depth. In *Self – Window*, we use stacked self-attention and feed-forward layers as a decoder without cross-attention to the encoder, i.e., a decoder-only design.

The *Cross – Window* module aggregates inter-frame information and infers metric depth by tracking changes of the same region across recording time. Temporally, we apply the module to windows in a backward incremental manner, proceeding from later to earlier frames until the first window. Theoretically, the mapping between blur change and depth is frame-count invariant; consequently, the window count governs invocation frequency but leaves the module’s weights solid.

Formally, the multi-frame features are embedded and processed through *Self – Window* and *Cross – Window* modules:

$$h_n^0 = \text{Embedding}(\{\phi_t\}_{t=(n-1)S}^{nS}), n = 1, \dots, T//S, \quad (5)$$

$$h_n^l = \text{Self – Window}^l(h_n^{l-1}), l = 1, \dots, L, \quad (6)$$

$$h_{n-1}^C = \text{Cross – Window}(h_n^C, h_{n-1}^L), n = T//S, \dots, 2, \quad (7)$$

where h_1^L is the final output after the attention computation and $h_{T//S-1}^C = \text{Cross – Window}(h_{T//S}^L, h_{T//S-1}^L)$. The final output head, composed of convolution layers and upsampling, compresses features to one channel and recovers the native spatial resolution to output the depth map L .

3.4 Trajectory Generation Algorithm.

Camera trajectory estimation proceeds in two stages: geometry-based inter-frame motion computation followed by attention-based dense trajectory generation. For the former stage, we take the tracker outputs Δ and the depth map L as inputs; for the latter, we further reuse the multi-frame features additionally.

Optics-based algorithm. The trajectory θ_t includes three angles (e.g., roll, pitch, yaw), corresponding to the camera’s three rotational DOFs. The algorithm computes roll, yaw, and pitch sequentially, since the latter angles are conditioned on the former.

We first determine the roll from the observed image rotation, since the induced delta is antisymmetric across the FOVs. Concretely, we compute the mean vertical offset p_y over all query points along $y = 0$ FOV. As the y-displacement on

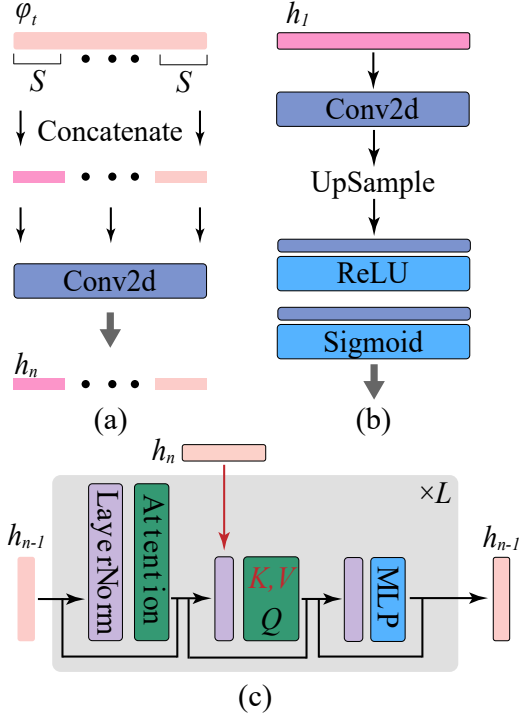


Figure 4: (a) **Window-embed.** Multi-frame features are windowed, concatenated along the channel dimension, and embedded with convolutional layer. (b) **Output head.** The head first reduces channels by half using a convolution, then upsamples via bilinear interpolation to the original resolution, and finally employs two convolution-activation stages to produce the depth map. (b) **Cross – Window.** Cross-attention is computed between two windows, where the refined post-window serves as the key-value to refine the pre-window.

this FOV is invariant to the x-field, this statistic yields the displacement with the roll component removed. Subtracting this mean from the previously offsets, we then combine the residuals with their coordinates to recover the roll angle. Subsequently, we consider the p_x of $x = 0$ FoV line. By subtracting, for each position, the displacement induced by the recovered roll motion, the remaining delta yields the yaw angle. Since the superposition of yaw and pitch contaminates p_y , only p_x remains discriminative for their estimation.

In the final step, we recover the pitch predominantly from p_y of all query points, leveraging the FoV coordinates in both x and y, together with the previously estimated yaw degree. The final output is formed via a weighted average across FOVs and weights are linearly tapered with field extent due to the aberration level increasing toward the periphery. Computational efficiency is improved via variable vectorization, i.e., rewriting the pipeline in matrix form to minimize per-sample loops. As the angles are defined post long-term temporal coupling, we resort to an optical computational method that sidesteps explicit disentanglement. Neural-network-based decoupling would be constrained by the practical difficulty of assembling a suitable dataset.

Dense trajectory decoder. For the dense trajectory estimation, we employ a text–image fusion paradigm in which linguistic information is integrated with visual representations to obtain trajectory fields.

Sparse trajectory are up-sampled using linear interpolation to ensure temporal consistency, after which the sequences are tokenized[51] for downstream modeling. Instead of window-embedding, we process the image features through the self-window block directly, after which we concatenate them with the final decoder output of the depth estimation part before output head. With both image and trajectory-text embeddings in hand, we leverage a vision–language framework to integrate the two, resulting in higher-precision dense trajectory fields.

While dense trajectory can, in theory, be inferred solely from multi-frame features, our experiments indicate that incorporating depth features (via concatenation) both speeds convergence and enhances reconstruction accuracy. Additionally, after upsampling of Θ , we ensure that the text sequence length matches the output sequence length, and no sampling is performed within the feed-forward layer.

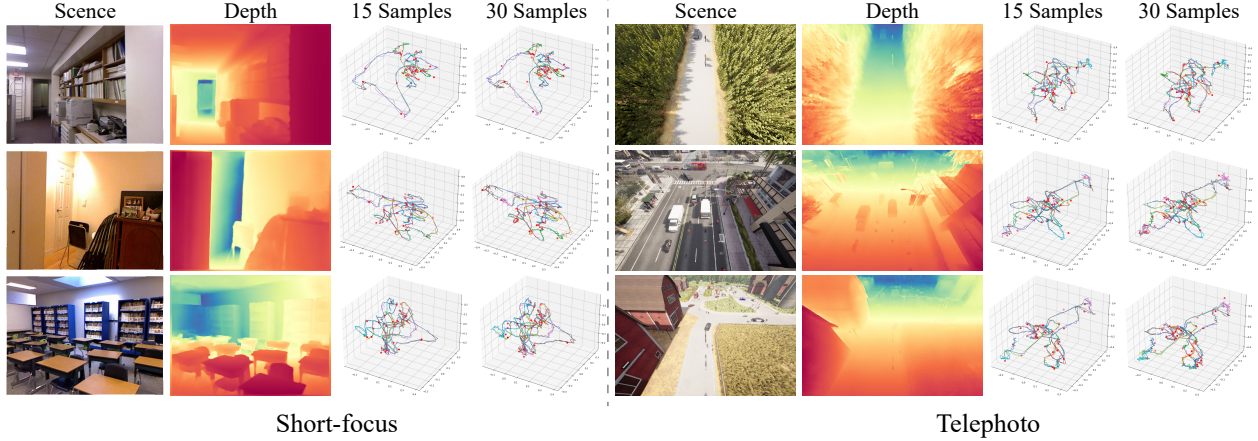


Figure 5: Results of our pipeline, including depth estimation and trajectory reconstruction. Here, samples denotes the number of samples within a single frame of the reconstructed dense trajectory. In the 3D plot, we render the GT trajectory as a blue solid line, depict the sparse trajectory with red markers, and use distinct colors to represent the reconstructed trajectory for each individual frame.

4 Experiment

4.1 Datasets and Evaluation Protocol

Datasets. Our scenario-oriented video data are derived from depth datasets through a imaging simulation pipeline based on Sec. 3.1. In order to cover a broad focal range and to model the distinct optical formulations of periscope telephoto systems, we employ indoor dataset NYU Depth[52] for short-focus camera and synthetic outdoor dataset SKYScenes[53] exhibiting a larger depth extent for telephoto one. Furthermore, leveraging a densely sampled camera motion and RGB–depth pairs, we produce videos with configurable exposure times and frame budgets, detailed in our supplementary material.

The camera trajectory is sourced from a gyroscope-recorded, long-duration handheld sequence with a 2-ms sampling interval as shown at the bottom left of Figure 1. Our trajectory sequence is 67.14 seconds long; we randomize the exposure onset for each video, constrained to preserve the prescribed exposure time. The video is rendered with a 60 ms per-row exposure, a 4 μ s per-row transfer time, and 30 frames overall. For NYU Depth dataset, we select 1,449 densely annotated images, with 200 scenes held out for validation. And in the SkyScenes dataset, we select ClearNoon scenes with heights between 15 m and 35 m and pitch angles from 0° to 60° . Post filtering, a set of 2,151 object-rich images is curated, from which 200 images are randomly selected to form the validation subset. The resulting corpus includes 3,200 training videos and 400 validation videos, both with its start-time of exposure. Samples are annotated as short-focus or telephoto camera, acknowledging that the optics-based algorithms in Sec. 3.4 differ.

Evaluation protocol. Within the pipeline, we perform separate training and validation for the depth estimation module in Sec. 3.3 and the trajectory estimation module in Sec. 3.4. Depth estimation is validated using established metrics and comparative baselines. In contrast, we measure the accuracy of the camera trajectory using following metrics.

We align the estimated dense camera trajectory to the simulated target one and report the L1 error over the trajectory samples. **AbsRel** is used to quantify proportional trajectory error, the same as depth part, L1 error over the target trajectory. To assess the accuracy of trajectory predictions under different thresholds, we utilize **Accuary** e_i , $i = 1, 2$, and unlike depth evaluation, the criterion mainly involves **AbsRel** instead of the ratio of the predicted trajectory to the target one.

4.2 Implementation Details

We decouple the training pipeline by optimizing depth estimation and trajectory estimation in two separate stages. For the former, we employ full-parameter training except the point tracker, whereas for the latter, all weights are frozen except those within the in Figure 3 (b). We train both stage using the AdamW optimizer[54] with a learning rate of 1×10^{-3} and a weight decay of 5×10^{-5} . The number of iterations in the two stages of training is 320K, with warm-up step of 1000. We employ one NVIDIA RTX 4090 GPU for training, with a batch size of 8. We use the number of Transformer layers, where layer has a hidden dimension of 384 and attention heads of 8, for *Self – Window*, *Cross – Window* and the trajectory decoder in Sec. 3.4 as $L = 6, 2, 6$, respectively. In dataset preparation, we standardize the input resolution to 518×518 ; for depth estimation, the temporal window parameter is configured as $S = 6$. For point tracker, we set the query points grid as 25×25 , $N = 625$ and conduct inference under the offline mode.

4.3 Main Results

Depth map results. We conduct a systematic evaluation of the proposed depth estimation method on three benchmarks; the quantitative metrics and comparative results are presented in Table 1. Two validation datasets are derived from our internally constructed validation set in Sec. 4.1. For the KITTI[55] benchmark, we identify 10 scenes featuring comparatively dense depth annotations and select several single high-clarity frames from each scene to synthesize videos, resulting in a total of 300 samples. For comparison, we apply single-image depth estimators[8, 7, 56, 57] to the first video frame, and, for video depth estimators[9, 10], we extract the first frame from their predictions, ensuring frame-aligned evaluation.

Table 1: **Quantitative results of depth map estimation.** The best one is emphasized using bold type, and the second one is indicated via underlined text.

Depth Estimator	NYU-D [52]			SKYScenes [53]			KITTI [55]			Average		
	AbsRel ↓	$\delta_1 \uparrow$	$\delta_2 \uparrow$	AbsRel ↓	$\delta_1 \uparrow$	$\delta_2 \uparrow$	AbsRel ↓	$\delta_1 \uparrow$	$\delta_2 \uparrow$	AbsRel ↓	$\delta_1 \uparrow$	$\delta_2 \uparrow$
<i>Single Image Depth Estimator</i>												
P3Depth [57]	0.104	0.898	0.981	0.155	0.817	0.898	0.071	0.953	0.993	0.110	0.889	0.957
IEBins [56]	0.087	0.936	0.992	0.130	0.849	0.912	<u>0.050</u>	<u>0.978</u>	0.998	0.089	0.921	0.967
ZoeDepth [7]	0.077	0.951	0.994	0.115	0.856	<u>0.950</u>	0.054	0.971	0.996	0.082	0.926	<u>0.980</u>
Depth-Anything (ViT-B) [8]	<u>0.063</u>	<u>0.977</u>	<u>0.997</u>	0.104	0.888	0.927	0.048	0.979	0.998	<u>0.072</u>	<u>0.948</u>	0.974
<i>Video Depth Estimator</i>												
DepthCrafter [9]	0.072	0.948	0.994	0.106	0.838	0.921	0.064	0.913	0.984	0.081	0.900	0.966
ChronoDepth [10]	0.070	0.936	0.992	<u>0.100</u>	0.871	0.948	0.073	0.956	0.992	0.081	0.921	0.977
(Ours)	0.054	0.989	0.998	0.095	<u>0.884</u>	0.953	0.051	<u>0.978</u>	0.998	0.067	0.950	0.983

Table 1 presents a comprehensive comparative study against competing approaches. For fairness, Depth-Anything is evaluated using its ViT-B model, which is aligned with the capacity of our DINO encoder. Our method outperforms other baselines in the NYU Depth dataset, while achieves strong results on SKYScenes and KITTI. The evidence suggests that the proposed method scales effectively to heterogeneous scenes and maintains competitive performance, underscoring its superior generalization and robustness. Nevertheless, in our prior expectation, synthetic datasets, which characterized by larger depth ranges and sharper depth discontinuities, would exhibit more pronounced blur patterns, thereby yielding superior estimation performance. We conjecture that the inverse experimental result is attributable to the limited FOV of telephoto optics, as the absence of wide-angle context reduces the available reference information.

Table 2: **Quantitative results of trajectory in different scale.** Θ is contrasted with canonical SfM methods, while the dense trajectory is validated against ground truth at different sampling densities. Post-interpolation refers to Θ after upsampling; the results indicate that our model yields a tangible gain in trajectory accuracy.

Methods	NYU-D [52]			SKYScenes [53]			KITTI [55]			Average		
	AbsRel ↓	$e_1 \uparrow$	$e_2 \uparrow$	AbsRel ↓	$e_1 \uparrow$	$e_2 \uparrow$	AbsRel ↓	$e_1 \uparrow$	$e_2 \uparrow$	AbsRel ↓	$e_1 \uparrow$	$e_2 \uparrow$
<i>Inter-frame Trajectory Θ</i>												
COLMAP [2]	0.486	0.228	0.262	0.581	0.212	0.270	0.489	0.263	0.338	0.519	0.234	0.290
DUST3R [3]	0.211	0.633	0.865	0.215	0.590	0.777	0.210	0.610	0.792	0.212	0.611	0.811
DiffusionSfM [4]	0.209	0.643	0.877	<u>0.161</u>	0.755	0.934	0.164	<u>0.748</u>	0.919	0.178	0.715	0.910
Ours + CoTracker[43]	0.045	0.933	1.000	0.043	0.978	1.000	0.045	0.967	1.000	0.044	0.959	1.000
<i>Dense Trajectory 15 per Frame</i>												
Post-interpolation	0.285	0.284	0.745	0.329	0.373	0.754	0.305	0.292	0.688	0.306	0.316	0.729
Ours + LocoTracker[39]	0.068	0.803	0.880	<u>0.069</u>	0.818	0.907	0.077	<u>0.745</u>	0.836	0.071	0.789	0.874
Ours + CoTracker[43]	0.064	0.865	0.949	0.070	0.858	<u>0.951</u>	0.070	0.851	<u>0.955</u>	0.068	0.858	<u>0.952</u>
<i>30 per Frame</i>												
Post-interpolation	0.315	0.353	0.719	0.402	0.196	0.575	0.313	0.218	0.657	0.343	0.256	0.650
Ours + LocoTracker[39]	0.066	0.825	0.908	0.067	0.841	0.925	0.071	0.790	0.878	<u>0.068</u>	0.819	0.904
Ours + CoTracker[43]	0.063	0.867	0.955	0.069	0.866	0.952	0.068	0.861	0.957	0.067	0.865	0.955

Trajectory results. The trajectory evaluation follows the same datasets as described above, with the ground truth defined by the trajectory curves in Figure 5. Due to scale discrepancies in the estimated results, we average the angle values within one frame for inter-frame trajectory; and for the 15 samples groups, we subsample the ground truth. Table 2 presents the comparisons against SfM methods, delineates the differences among trackers, and quantifies the performance gains contributed by our dense trajectory decoder. Although post-averaging inter-frame trajectory may introduce deviations from the true values, our method substantially outperforms competing approaches. Regarding the tracker, CoTracker[43] exhibits a measurable advantage over LocoTracker[39]; accordingly, we adopt the former in our pipeline.

4.4 Ablation Studies

We present our ablation studies on Table 3. We first ablate the design effectiveness of the depth estimation stage. In (I), the window size is systematically adjusted, encompassing reduced-length and extended-length settings. As changing S alters the number of concatenated features, we accordingly adjust the convolutional layer configuration during training. In (II), we ablate the *Cross – Window* mechanism by removing it and directly feeding the output of *Self – Window*, into the output head. In (III), we evaluate varying number of Transformer layers in our dense trajectory decoder. The observed performance degradation demonstrates the effectiveness of our pipeline design. Specifically, in (I), shorter S yield superior performance compared to longer one. In (II), removing the *Cross – Window* module substantially degrades depth accuracy and, in turn, diminishes the quality of the trajectory reconstruction. Finally, (III) shows that: within 6 layers, reducing the depth of the network consistently degrades performance; therefore, balancing accuracy with model size, we set the number of layers as 6.

Table 3: **Ablation studies.** We evaluate performance of different baselines on both depth estimation and trajectory metrics.

Average Metrics	(I) S		(II) cross		(III) L			Ours
	4	8	3	4	5			
$\delta_1 \uparrow$	0.946	0.923	0.887	-	-	-	0.950	
AbsRel \downarrow	0.071	0.078	0.091	0.082	0.077	0.073	0.067	
$e_1 \uparrow$	0.862	0.812	0.810	0.783	0.845	0.863	0.865	

5 Conclusion

We introduce a novel perspective-blur-based framework for depth estimation and trajectory densification that utilizing blur cues and temporal image variations present in video sequences. Leveraging attention-based encoder and decoders, we reconstruct single, dense metric depth map and infer the corresponding camera trajectory directly from monocular video input. This approach offers substantial utility in scenarios necessitating dense camera pose information, for instance, in assessing camera stabilization. We aspire for this work to inspire the community to pursue broader innovation and exploration in related fields.

References

- [1] G. Page. Multiple view geometry in computer vision, by richard hartley and andrew zisserman, cup, cambridge, uk, 2003, vi+560 pp., isbn 0-521-54051-8. *Robotica*, 23:271, 03 2005.
- [2] Johannes Schönberger and Jan-Michael Frahm. Structure-from-motion revisited. 06 2016.
- [3] Shuzhe Wang, Vincent Leroy, Yohann Cabon, Boris Chidlovskii, and Jerome Revaud. Dust3r: Geometric 3d vision made easy. In *CVPR*, 2024.
- [4] Qitao Zhao, Amy Lin, Jeff Tan, Jason Y. Zhang, Deva Ramanan, and Shubham Tulsiani. Diffusionsfm: Predicting structure and motion via ray origin and endpoint diffusion. In *CVPR*, 2025.
- [5] Xiaoyan Wang, Tang Yi, Qiuyan Tang, Liang Feng, Guoqiang Ni, and Liwei Zhou. Simulation and Analysis of Vibration Blurred Images. In *2010 International Conference on Computational Intelligence and Software Engineering*, pages 1–4, Chengdu City, China, September 2010. IEEE.
- [6] Tianchen Qiu, Jingwen Zhou, Huajun Feng, Qi Li, Tongyue Li, and Yueting Chen. Imaging simulation and restoration for a mobile-based long-focus camera with optical stabilization. *Applied Optics*, 63(19):F80, July 2024. Publisher: Optica Publishing Group.

- [7] Shariq Farooq Bhat, Reiner Birkl, Diana Wofk, Peter Wonka, and Matthias Müller. Zoedepth: Zero-shot transfer by combining relative and metric depth, 2023.
- [8] Lihe Yang, Bingyi Kang, Zilong Huang, Xiaogang Xu, Jiashi Feng, and Hengshuang Zhao. Depth anything: Unleashing the power of large-scale unlabeled data. In *CVPR*, 2024.
- [9] Wenbo Hu, Xiangjun Gao, Xiaoyu Li, Sijie Zhao, Xiaodong Cun, Yong Zhang, Long Quan, and Ying Shan. Depthrafter: Generating consistent long depth sequences for open-world videos. In *CVPR*, 2025.
- [10] Jiahao Shao, Yuanbo Yang, Hongyu Zhou, Youmin Zhang, Yujun Shen, Vitor Guizilini, Yue Wang, Matteo Poggi, and Yiyi Liao. Learning temporally consistent video depth from video diffusion priors, 2024.
- [11] Seokju Cho, Jiahui Huang, Seungryong Kim, and Joon-Young Lee. Seurat: From moving points to depth, 2025.
- [12] Maxime Oquab, Timothée Darcet, Théo Moutakanni, Huy Q. Vo, Marc Szafraniec, Vasil Khalidov, Pierre Fernandez, Daniel Haziza, Francisco Massa, Alaaeldin El-Nouby, Mahmoud Assran, Nicolas Ballas, Wojciech Galuba, Russ Howes, Po-Yao (Bernie) Huang, Shang-Wen Li, Ishan Misra, Michael G. Rabbat, Vasu Sharma, Gabriel Synnaeve, Huijiao Xu, Hervé Jégou, Julien Mairal, Patrick Labatut, Armand Joulin, and Piotr Bojanowski. Dinov2: Learning robust visual features without supervision. *ArXiv*, abs/2304.07193, 2023.
- [13] Shiqi Chen, Huajun Feng, Keming Gao, Zhihai Xu, and Yuetong Chen. Extreme-quality computational imaging via degradation framework. In *Proceedings of the IEEE/CVF International Conference on Computer Vision (ICCV)*, pages 2632–2641, October 2021.
- [14] Shiqi Chen, Ting Lin, Huajun Feng, Zhihai Xu, Qi Li, and Yuetong Chen. Computational optics for mobile terminals in mass production. *IEEE Transactions on Pattern Analysis and Machine Intelligence*, 45(4):4245–4259, April 2023.
- [15] H. C. Longuet-Higgins. A computer algorithm for reconstructing a scene from two projections. *Nature*, 293(5828):133–135, September 1981.
- [16] Olivier Faugeras. Three-dimensional computer vision: a geometric viewpoint. *MIT press*, 01 1993.
- [17] B. Triggs, Philip McLauchlan, R. Hartley, and Andrew Fitzgibbon. Bundle adjustment - a modern synthesis. *ICCV '99 Proceedings of the International Workshop on Vision Algorithms: Theory and Practice*, pages 198–372, 01 2000.
- [18] Noah Snavely, Steven Seitz, and Richard Szeliski. Photo tourism: Exploring photo collections in 3d. *ACM Transactions on Graphics (2006)*, 25:835–846, 01 2006.
- [19] Changchang Wu. Towards linear-time incremental structure from motion. pages 127–134, 06 2013.
- [20] Martin A. Fischler and Robert C. Bolles. Random sample consensus: a paradigm for model fitting with applications to image analysis and automated cartography. *Commun. ACM*, 24:381–395, 1981.
- [21] R.I. Hartley. In defense of the eight-point algorithm. *IEEE Transactions on Pattern Analysis and Machine Intelligence*, 19(6):580–593, 1997.
- [22] Manolis Lourakis and Antonis Argyros. Sba: A software package for generic sparse bundle adjustment. *ACM Trans. Math. Softw.*, 36, 01 2009.
- [23] David Crandall, Andrew Owens, Noah Snavely, and Dan Huttenlocher. Discrete-continuous optimization for large-scale structure from motion. In *CVPR 2011*, pages 3001–3008, 2011.
- [24] Chris Sweeney, Tobias Höllerer, and Matthew Turk. Theia: A fast and scalable structure-from-motion library. pages 693–696, 10 2015.
- [25] Pierre Moulon, Pascal Monasse, Romuald Perrot, and Renaud Marlet. Openmvg: Open multiple view geometry. pages 60–74, 04 2017.
- [26] Xingkui Wei, Yinda Zhang, Zhuwen Li, Yanwei Fu, and Xiangyang Xue. *DeepSFM: Structure from Motion via Deep Bundle Adjustment*, pages 230–247. 11 2020.
- [27] Chengzhou Tang and Ping Tan. Ba-net: Dense bundle adjustment network. *ArXiv*, abs/1806.04807, 2018.
- [28] Vincent Leroy, Yohann Cabon, and Jerome Revaud. Grounding image matching in 3d with mast3r, 2024.
- [29] Chen-Hsuan Lin, Wei-Chiu Ma, Antonio Torralba, and Simon Lucey. Barf: Bundle-adjusting neural radiance fields. In *IEEE International Conference on Computer Vision (ICCV)*, 2021.
- [30] Jianyuan Wang, Nikita Karaev, Christian Rupprecht, and David Novotny. Vggsfm: Visual geometry grounded deep structure from motion. pages 21686–21697, 06 2024.
- [31] Iain Matthews and Simon Baker. Active appearance models revisited. *International Journal of Computer Vision*, 60, 03 2004.

- [32] Jianbo Shi and Carlo Tomasi. Good features to track. *Proceedings / CVPR, IEEE Computer Society Conference on Computer Vision and Pattern Recognition. IEEE Computer Society Conference on Computer Vision and Pattern Recognition*, 600, 03 2000.
- [33] Bruce Lucas and Takeo Kanade. An iterative image registration technique with an application to stereo vision (ijcai). volume 81, 04 1981.
- [34] Berthold Horn and Brian Schunck. Determining optical flow. *Artificial Intelligence*, 17:185–203, 08 1981.
- [35] J.-Y. Bouguet. Pyramidal implementation of the lucas kanade feature tracker. 1999.
- [36] David G. Lowe. Distinctive image features from scale-invariant keypoints. *International Journal of Computer Vision*, 60:91–110, 2004.
- [37] Ethan Rublee, Vincent Rabaud, Kurt Konolige, and Gary Bradski. Orb: an efficient alternative to sift or surf. pages 2564–2571, 11 2011.
- [38] Daniel DeTone, Tomasz Malisiewicz, and Andrew Rabinovich. Superpoint: Self-supervised interest point detection and description. pages 337–33712, 06 2018.
- [39] Seokju Cho, Jiahui Huang, Jisu Nam, Honggyu An, Seungryong Kim, and Joon-Young Lee. Local all-pair correspondence for point tracking. *arXiv preprint arXiv:2407.15420*, 2024.
- [40] Carl Doersch, Ankush Gupta, Larisa Markeeva, Adrià Recasens, Lucas Smaira, Yusuf Aytar, João Carreira, Andrew Zisserman, and Yezhou Yang. Tap-vid: A benchmark for tracking any point in a video. *ArXiv*, abs/2211.03726, 2022.
- [41] Meike Nauta, Jörg Schlötterer, Maurice van Keulen, and Christin Seifert. Pip-net: Patch-based intuitive prototypes for interpretable image classification. In *2023 IEEE/CVF Conference on Computer Vision and Pattern Recognition (CVPR)*, pages 2744–2753, 2023.
- [42] Carl Doersch, Yi Yang, Mel Vecerík, Dilara Gokay, Ankush Gupta, Yusuf Aytar, João Carreira, and Andrew Zisserman. Tapir: Tracking any point with per-frame initialization and temporal refinement. *2023 IEEE/CVF International Conference on Computer Vision (ICCV)*, pages 10027–10038, 2023.
- [43] Nikita Karaev, Ignacio Rocco, Benjamin Graham, Natalia Neverova, Andrea Vedaldi, and Christian Rupprecht. Cotracker: It is better to track together. In *Proc. ECCV*, 2024.
- [44] Hongyang Li, Hao Zhang, Shilong Liu, Zhaoyang Zeng, Tianhe Ren, Feng Li, and Lei Zhang. TAPTR: Tracking Any Point with Transformers as Detection. In *European Conference on Computer Vision*, pages 57–75, 2024.
- [45] Ilya Tolstikhin, Neil Houlsby, Alexander Kolesnikov, Lucas Beyer, Xiaohua Zhai, Thomas Unterthiner, Jessica Yung, Andreas Steiner, Daniel Keysers, Jakob Uszkoreit, Mario Lucic, and Alexey Dosovitskiy. Mlp-mixer: an all-mlp architecture for vision. In *Proceedings of the 35th International Conference on Neural Information Processing Systems, NIPS '21*, 2021.
- [46] Ashish Vaswani, Noam M. Shazeer, Niki Parmar, Jakob Uszkoreit, Llion Jones, Aidan N. Gomez, Łukasz Kaiser, and Illia Polosukhin. Attention is all you need. In *Neural Information Processing Systems*, 2017.
- [47] Zhengqi Li and Noah Snavely. Megadepth: Learning single-view depth prediction from internet photos. *2018 IEEE/CVF Conference on Computer Vision and Pattern Recognition*, pages 2041–2050, 2018.
- [48] René Ranftl, Katrin Lasinger, David Hafner, Konrad Schindler, and Vladlen Koltun. Towards robust monocular depth estimation: Mixing datasets for zero-shot cross-dataset transfer. *IEEE Transactions on Pattern Analysis and Machine Intelligence*, 44(3), 2022.
- [49] Ravi Garg, B. V. Kumar, G. Carneiro, and Ian D. Reid. Unsupervised cnn for single view depth estimation: Geometry to the rescue. In *European Conference on Computer Vision*, 2016.
- [50] Robin Rombach, A. Blattmann, Dominik Lorenz, Patrick Esser, and Björn Ommer. High-resolution image synthesis with latent diffusion models. *2022 IEEE/CVF Conference on Computer Vision and Pattern Recognition (CVPR)*, pages 10674–10685, 2021.
- [51] Pengcheng He, Xiaodong Liu, Jianfeng Gao, and Weizhu Chen. Deberta: Decoding-enhanced bert with disentangled attention. In *ICLR*, 2021.
- [52] Pushmeet Kohli, Nathan Silberman, Derek Hoiem, and Rob Fergus. Indoor segmentation and support inference from rgbd images. In *ECCV*, 2012.
- [53] Sahil Khose, Anisha Pal, Aayushi Agarwal, Deepanshi, Judy Hoffman, and Prithvijit Chattopadhyay. Skyscenes: A synthetic dataset for aerial scene understanding. In *European Conference on Computer Vision*, 2025.
- [54] Ilya Loshchilov and Frank Hutter. Decoupled weight decay regularization. In *International Conference on Learning Representations*, 2017.

- [55] Andreas Geiger, Philip Lenz, Christoph Stiller, and Raquel Urtasun. Vision meets robotics: The kitti dataset. *International Journal of Robotics Research (IJRR)*, 2013.
- [56] Shuwei Shao, Zhongcai Pei, Xingming Wu, Zhong Liu, Weihai Chen, and Zhengguo Li. Iebins: Iterative elastic bins for monocular depth estimation. In *Advances in Neural Information Processing Systems (NeurIPS)*, 2023.
- [57] Vaishakh Patil, Christos Sakaridis, Alex Liniger, and Luc Van Gool. P3depth: Monocular depth estimation with a piecewise planarity prior. In *Proceedings of the IEEE/CVF Conference on Computer Vision and Pattern Recognition (CVPR)*, 2022.